PLANETARY SCIENCE

Hypervelocity impacts as a source of deceiving surface signatures on iron-rich asteroids

Guy Libourel[1,2]*, Akiko M. Nakamura[3], Pierre Beck[4], Sandra Potin[4], Clément Ganino[5], Suzanne Jacomet[6], Ryo Ogawa[3], Sunao Hasegawa[7], Patrick Michel[1]

Several arguments point to a larger proportion of metal-rich asteroids than that derived from spectral observations, as remnants of collisional disruptions of differentiated bodies. We show experimentally that this apparent deficit may result from the coating of metallic surfaces by silicate melts produced during impacts of hydrated or dry projectiles at typical asteroid impact speeds. Spectral analysis of steel and iron meteorite targets after impact shows a profoundly modified optical signature. Furthermore, hydrated projectiles leave a 3-μm absorption hydration feature. This feature is thus consistent with a metallic surface and does not require an unusual low-speed impact. Unless systematizing radar measurements, ground-based spectral observations can be deceptive in identifying iron-rich bodies. The NASA Psyche mission rendezvous with Psyche will offer the unique opportunity both to measure the relative abundances of regolith and glassy coated surfaces and to substantially increase our understanding of impact processes and signatures on a metal-rich asteroid.

INTRODUCTION

Recent measurements using the ^{182}Hf/^{182}W isotopic chronometer on iron meteorites (1, 2) have shown that a notable fraction of planetesimals experienced silicate-metal differentiation within the first million years after the formation of the solar system. Powered by ^{26}Al decay, the first generations of accreted bodies had to differentiate, and these objects should exist among the asteroid population (3). While some objects are preserved relatively pristine, such as Vesta (4, 5), catastrophic impacts are believed to have revealed the metallic cores of many of these bodies, and several classes of iron-rich meteorites have been identified on Earth. Around 50 to 60 individual metallic asteroids (6) are expected to explain the geochemistry of ungrouped and grouped iron meteorites (7, 8). Their very long cosmic ray exposure ages (9) indicate, however, that these collisions occurred long ago, i.e., from hundreds of millions to a few billion years ago.

Spectral observations of asteroids show, however, a deficit of metal-rich objects in the asteroid belt. In effect, visible and near-infrared (VIS-NIR) surveys have led to classification of only a limited number of asteroids in the M taxonomic class, which historically has been thought to correspond to the denuded metallic cores of disrupted parent bodies or possibly enstatite chondrites (10–13). There is a large variety of spectral behaviors for these objects, as their spectra are extended into the near-infrared, with absorption bands tentatively attributed to pyroxene and/or hydrous silicates in many of them

(14–17). It has also been found (18–20) that only 30 to 40% of the M-class asteroids have radar albedos consistent with metal-dominated composition. The remaining 60 to 70% have surface regolith bulk densities higher than is typical of other main belt asteroids (19) and are likely to be metal-rich but not dominated by metal. Therefore, either most of the metal has disappeared by complete disruptions (21) or the lack of metal-rich asteroids is only apparent. Increased understanding of metal-rich asteroid surfaces, which, until now, have remained poorly characterized, will make a giant step forward with the visit of the NASA Psyche mission to the asteroid Psyche in 2026 (22).

It has been proposed that the apparent paucity of metal-rich asteroids based on spectral observations is due to collisions that may deposit foreign material on their surfaces (14), thus hiding or altering their metallic characteristics and consequently biasing their spectral classification. The idea that low-velocity collisions have modified the spectral characteristics of M-class asteroids was later invoked to explain the apparent incongruity of a metallic radar signature and a hydrated spectral signature seen on a variety of M-class asteroids (23). It was then convincingly demonstrated that the expression of dark material on the surface of Vesta is the result of low-velocity collisions with one or more primitive objects (24). A similar scenario has also been invoked for Ceres surface with a partial contamination by exogenous enstatite-rich material, possibly coming from the Beagle asteroid family (25). However, in the asteroid belt, low-speed collisions are rare. During their lifetime, all asteroids instead experience hypervelocity impacts with a range of projectile sizes, with typical impact speeds of about 5 km/s (26). Craters are thus produced on asteroid surfaces, as evidenced by a plethora of space mission images. Looking for a more generic/robust scenario accounting for the most likely impact speeds in the asteroid belt (25), we conducted a campaign of hypervelocity impact experiments on metallic targets using representative impact speeds.

RESULTS

Hypervelocity impact experiments

A series of impact experiments, all shot vertically to the target surface, have been conducted using steel and Gibeon iron meteorite

[1]Université Côte d'Azur, Observatoire de la Côte d'Azur, CNRS, Laboratoire Lagrange, Boulevard de l'Observatoire, CS 34229, 06304 Nice Cedex 4, France. [2]Hawai'i Institute of Geophysics and Planetology, School of Ocean, Earth Science and Technology, University of Hawai'i at Mānoa, Honolulu, HI 96821, USA. [3]Graduate School of Science, Kobe University, 1-1 Rokkoudai-cho, Nada-ku, Kobe 657-8501, Japan. [4]UJF-Grenoble 1/CNRS-INSU, Institut de Planétologie et d'Astrophysique de Grenoble (IPAG) UMR 5274, Grenoble F-38041, France. [5]Université Côte d'Azur, Observatoire de la Côte d'Azur, CNRS, Laboratoire Géoazur, 250 rue Albert Einstein, Sophia-Antipolis, 06560 Valbonne, France. [6]MINES Paristech, PSL-Research University, CEMEF-Centre de Mise en Forme des Matériaux/Centre for Material Forming, CNRS UMR 7635, CS 10207, 1 rue Claude Daunesse, 06904 Sophia-Antipolis Cedex, France. [7]Institute of Space and Astronautical Science, Japan Aerospace Exploration Agency, 3-1-1 Yoshinodai, Chuo-ku, Sagamihara 252-5210, Japan.
*Corresponding author. Email: libou@oca.eu

targets as proxies of metal-rich asteroids (27, 28). Dry versus hydrated glassy basalt and crystallized dunite samples have been used as projectiles to mimic the diversity of asteroid materials, i.e., (carbonaceous) primitive or differentiated, hydrated, or dry bodies. Eleven experimental runs were performed with increasing impact speed from 3.39 to 6.89 km/s and different masses of projectile from 0.03 to 0.08 g, resulting in different impact energies (see table S1). The impact is captured with a high-speed video camera that monitors the experiment. The compositions of impact craters were then characterized by using scanning electron microscopy (SEM) observations and energy-dispersive x-ray diffraction chemical maps, as well as by VIS-NIR spectral analysis of the crater floor of the metallic target (see Materials and Methods for experimental and analytical conditions).

Irrespective of the nature of the target and the projectile, our results (Figs. 1 to 3) show that the size of the craters produced by hypervelocity impacts is in the range of 6 to 10 mm, consistent with predictions by classical scaling rules (29, 30). The crater's morphology with a bowl-like shape (29, 30) is also typical of normal and oblique (up to 45° impact angle) hypervelocity impacts (31). An almost continuous frozen metallic lip that rises at the edge of the crater (29) surrounds all craters produced in this set of experiments (Figs. 1 and 2). It is noticeable, however, that the crater's metallic rims on iron meteorite targets are more irregular and protruding than their equivalent on steel targets. The immediate vicinity of craters is deformed and bended toward the crater rims on the steel targets, whereas they are both deformed and fractured on the iron meteorite targets (Figs. 1 and 2 and sections S3 to S6). There is no notable difference in the crater's morphology between those produced by impacts on Gibeon targets set either at low temperature or at room temperature.

For all impact speeds, x-ray chemical maps indicate that the metallic crater floor is covered by a thin, more or less continuous, layer of impact melt (now glassy) mainly made of projectile material (Fig. 1). The coating covers the entire inner surface of craters in both steel and iron meteorite targets, including the walls to the crater's rims (Figs. 1 and 2 and sections S4 and S5). The coating is glassy and free of any crystalline phases, irrespective of the tested impact speed (table S1) and of the nature of the target (iron meteorite or steel) and the impactor (dunite or basalt, crystallized, or glassy). No unmelted fragments of projectiles have been observed trapped within the glasses. The glassy coating is formed by a network of centro-radial-anastomosed channels with the Fe metal substrate (Figs. 1 and 2 and section S4). In all the studied craters (Fig. 3 and sections S4 and S5), the surface coating is constituted of a vesicular or frothy carapace, such as scoria or pumice, in response to the adiabatic decompression of the impact melt and the quenching of the melt-gas mixture. Because of its layout in the form of channels and tears, the coating has an irregular thickness varying from 0 to about ≈100 μm (Figs. 1 to 3), which corresponds to about 10% of the initial volume of the projectile. Basalt coatings are, on average, thicker than their dunite counterparts, very likely in response to the higher viscosity of basaltic melt (one to two orders of magnitude difference) and their different wetting properties on iron metal substrates. It is also remarkable that the coating in the highest impact speed experiments (e.g., #103 using a dunite projectile) consists of a frozen emulsion of metal-silicate immiscible liquids, similar to an oil-water mixture (Fig. 3 and section S4). Detailed x-ray images and cross sections of craters confirm the occurrence of countless metal pools and beads

from several tens of micrometers to a few nanometers inside glassy coatings (Fig. 1 and section S3). They are associated with larger shapeless target metal fragments, which are very likely ripped out from the crater's bottom. A high-speed video camera (frame rate of 2 or 4 μs) that monitors the impact confirmed the occurrence in the ejecta population of millimeter-sized shapeless metal spalls excavated from the target (section S1).

Spallation and fracturing are the other characteristics of the studied impact craters on both types of targets. Spall fracture planes on the crater rims and spall fractures in cross section near the crater rims are observed (section S4). Fractures can be seen by SEM images taken from the crater's top view in both steel and iron meteorite targets (Figs. 1 and 2 and sections S4 to S6). They are concentrically arranged in craters, forming curved scales of variable thickness. From the cross section of a steel crater (Fig. 2B), fractures concentrate at the crater's bottom, generating a highly fractured and highly porous metal zone below the crater floor. Fractures parallel the impact direction of the projectile below the crater and propagate at a depth equivalent to the crater's depth below the crater floor within the metallic target. All these microstructures and microdamages are indicative of dynamic failures. They are similar to other dynamic failures observed on steel under hypervelocity impacts (31, 32).

Some fractures are injected by the impact melt, and others are not (Fig. 1, D and E, and section S3). Some of these fractures and voids, which are apparent in the crater's bottom and are very likely produced during the crater excavation stage, are also empty of melt and correspond to an open porosity (Fig. 1D). These two sorts of fractures (open and filled with melt) contribute to a certain reduction of the near-subsurface metallic target's density. Thin glass threads often connect the two rims of the same concentric fracture in craters, suggesting that the formation and the opening of the fractures are necessarily before the quenching of the impact melt (Fig. 3A).

VIS-NIR spectral observations

To compare our hypervelocity impact craters with pitted or cratered surfaces of metal-rich asteroids, VIS-NIR spectral analyses of steel (Fig. 4A) and iron meteorite (Fig. 4B) targets after impact have been undertaken. Spectra were measured under nadir illumination and emergence angle of 20° to 30° (see Materials and Methods). It has been shown that, from sections of metallic surfaces of steel or iron meteorites, the effects of compaction, porosity, and particle size are not critical parameters (33). However, changes in surface roughness significantly affect the brightness and spectra of metallic surfaces (section S1).

The starting material with a polished surface displays a blue slope typical of metallic material when observed outside of the specular or quasi-specular direction (33). Spectra were also measured within the craters, with an illuminated area slightly smaller than the crater size (7 mm in diameter). All crater spectra present a spectral signature very distinct from the starting material, with the appearance of a strong red slope (Fig. 4, A and B), typical of specular reflection on metallic surfaces (33). This behavior can be interpreted by the geometry of the crater, where the hemispherical depression is favorable to the presence of specular reflection (red sloped) when illuminated at low phase angles. This "crater morphology effect" is combined to the development of small-scale (1 to 10 μm) roughness within the crater, which also increases the contribution of specular reflection and contributes to the red slope. To model the latter effect, the influence of small-scale roughness was investigated by progressively
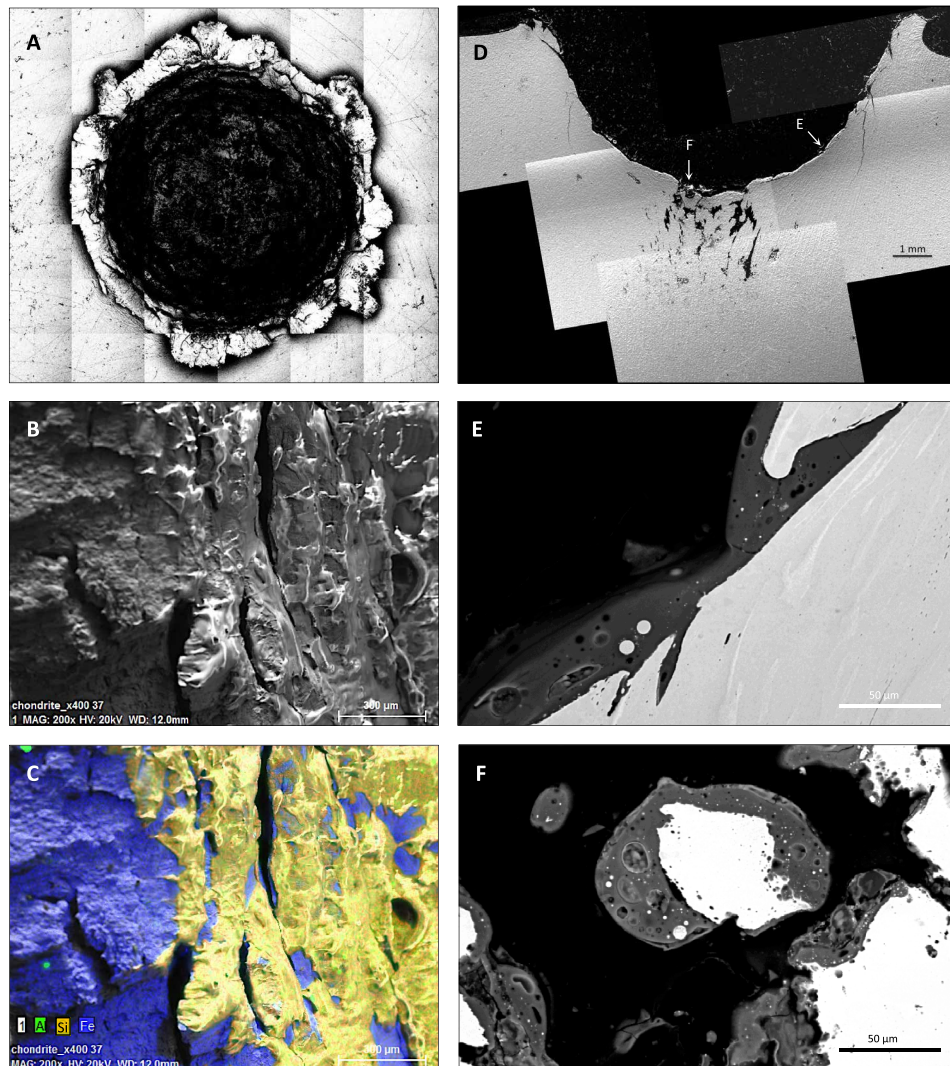
Fig. 1. Features and characteristics of craters generated by our hypervelocity impact experiments on steel metallic targets. (**A**) Secondary electron microscopy (SEM) images of the target taken orthogonal to the section of the n0 crater (6.89 km/s; 1899 J). This representative example (*27*) shows that craters have the typical regular bowl shape surrounded by an almost continuous frozen metallic lip that rises at the edge of the crater. Note that the bottom of the crater backscatters electrons less efficiently than the unprocessed metallic surface (and thus appears darker in the image). This is explained by the low average atomic number of the basaltic-like impact melt coating in the processed area of the target. (**B**) Vertical SEM image of the inside edge of the n4 crater (6.88 km/s; 710 J) depicting the impact melt coating with glassy and degassing features. (**C**) Composite x-ray element map (Al, green; Fe, blue; Si, red) of the same area of the n4 crater (6.88 km/s; 710 J). Note that the coating spreads efficiently over the entire surface of the bowl shape crater [modified from previous work (*27*)]. (**D**) Secondary electron–SEM image of a cross section of the n0 crater (6.89 km/s; 1899 J) showing a regular, almost symmetrical concave section. Concentric fractures are apparent from the top down to the bottom of the crater. There is a strong concentration of fractures and voids at the bottom of the crater, which produces a substantial increase of porosity at a depth well below the crater's bottom. Notice shear bands and the occurrence of crystal-oriented texture in the steel. (**E**) Electron backscattered SEM image showing the basalt-like impact melt coating of the crater surface on its sides, with a thickness of a few tens of micrometers [see (D) for location]. The creation of fracture areas by the injection of the melt is observable. Note that the basaltic melt is spotted with minute metallic blebs and gas bubbles. Target metal is highly deformed. (**F**) Electron backscattered SEM image of the crater bottom [see (D) for location]. In addition to the minute metallic blebs and bubbles shown in (E), large metal chips that are extracted from the metallic target during the impact are shown.

roughening a polished surface of the Gibeon meteorite, with SiC discs (figs. S2 and S3). These measurements enabled us to reproduce the evolution from blue-sloped spectra (as measured on the polished area outside of the crater) to red-sloped ones (as measured inside the crater).

Combined with these purely geometric effects, the presence of a silicate glass draping the crater also modifies the spectral signature. One of the produced craters on a steel target (n5) was treated with a mixture of hydrofluoric acid and nital to remove the dunite impact melt coating. The spectra measured before and after chemical treatment revealed that removing the silicate coating increases the spectral slope and increases the overall reflectance (Fig. 5A). This experience shows that the outcome of the cratering process can alter the optical signature of metallic surfaces and could complicate their detection of these surfaces using spectroscopic data.

The spectral analysis of the craters leads to other interesting outcomes. First, the impact crater produced using a dunite impactor does not show any signature of olivine (band at 1.1 μm), suggesting
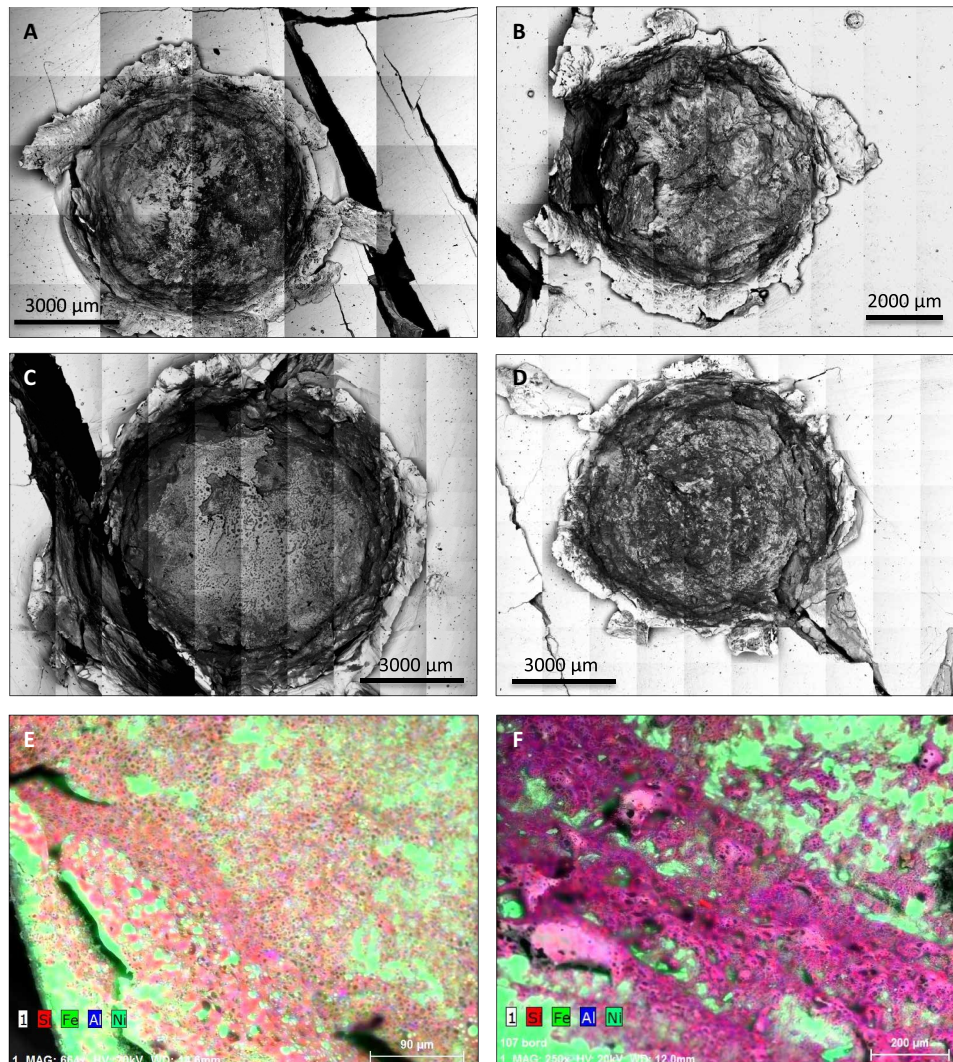
Fig. 2. Electron backscattered (BSE) characteristic images of craters generated by hypervelocity impact experiments on the Gibeon iron meteorite target chunks using both dunite and basalt projectiles. (**A**) #101 dunite at 3.25 km/s at room temperature. The crater's morphology is a typical bowl-like shape with a clear darkening of its interior. Notice that the crater's metallic rims are irregular and largely protruding. (**B**) #102 dunite at 3.28 km/s at 151 K. This bowl-like shape crater is obtained in the same experimental conditions than run #101, but the dwell target temperature was set at 151 K. Similar features are observable, except the tearing off part of the crater wall on its left part (see section S6). (**C**) #103 dunite at 6.97 km/s at room temperature. This is the higher-velocity impact crater obtained with a dunite projectile. Its interior consists of a frozen emulsion of metal-silicate immiscible liquids. (**D**) #107 basalt at 5.08 km/s at 131 K. The darkening of the inside of the crater is more pronounced than in the other impact experiments using dunite as a projectile. Concentric cracks are also present. (**E**) Electron backscattered SEM image showing the dunite-like glassy coating (pink) of the run #103 iron crater surface (green) on its sides. The glassy coating contains numerous bubbles. (**F**) Electron backscattered SEM image showing the basalt-like glassy coating (pink) of the #107 crater. Notice here the heterogeneous thickness of the glassy coating and its foamy texture (iron-rich materials are in green).

the efficiency of impacts to completely melt olivine-rich rocks—these results being largely independent of velocity, target, and impact materials (at least for the samples tested here). Second, in the case of the crater produced using a basaltic impactor on the Gibeon meteorite, large absorption can be detected around 1 and 2 µm. The position and relative intensities of these bands can be interpreted by the presence of Fe^{2+} in a silicate glass. VIS-NIR spectra of multiple Fe-rich basaltic glasses [16.66 to 22.95 weight % (wt %) FeO] created at a wide range of oxygen fugacity were studied by Bell *et al.* (*34*), and each glass had absorptions near 1.0 and 2.0 µm, likely owing to crystal field and charge transfer transitions within the glasses. These

two bands were also observed in the study of Fe^{2+}-bearing glasses by Cloutis (*35*). These bands are, however, much less resolved in the impact melts produced by dunite projectiles by comparison with those produced by basaltic projectiles in response to their higher depolymerized melt/glass structure. These experiments thus reveal that in addition to altering the optical signatures, hypervelocity impacts can also imprint new absorption features.

Last, reflectance spectra acquired from hypervelocity experiments in the range of 5 km/s using dry versus hydrated basaltic projectiles (Fig. 6) reveal that the impact glass in the crater produced by hydrated impact projectiles exhibits a clear 3-µm absorption feature
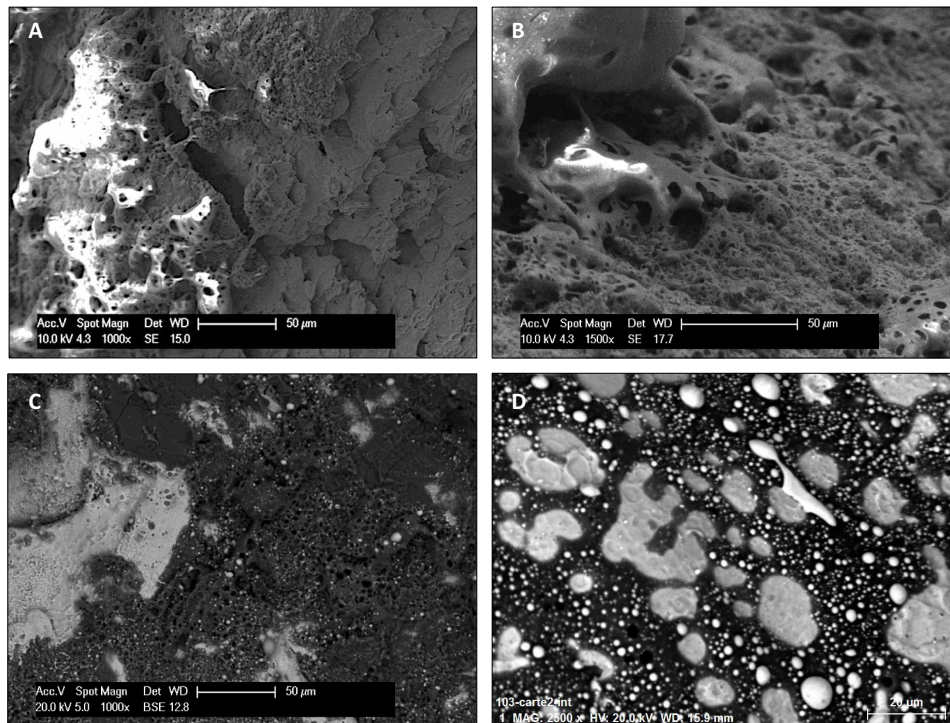
Fig. 3. SEM images of glassy coating in impact craters. (**A**) Thin glass threads connecting the two rims of the same concentric fracture in the n4 crater, suggesting that the formation and the opening of the fractures are necessarily before the quenching of the impact melt. (**B**) Secondary electron images of the frothy and foamy bottom of the crater NW2. (**C**) BSE view of the bottom of the n5 crater dunite resulting from the impact of a dunite projectile at 4.91 km/s and showing a vesicular impact coating constituted by a mixture of dunite (dark) and iron (light) materials. (**D**) Detail of the #103 crater interior resulting from the impact of a dunite projectile at 6.97 km/s and showing a frozen emulsion of metal (light color)–silicate (dark color) immiscible liquids.

attributed to the absorption of hydroxyl by the glassy coating. By serendipity, this entrapment of water, as hydroxyl species within impact glasses, is further confirmed by our hypervelocity impact experiments performed at low temperature (table S1), in which the residual water moisture of the experimental chamber, condensed at the Gibeon iron meteorite surfaces before the shots, is trapped in the impact glasses, as revealed by the occurrence of a 3-μm absorption band in the corresponding spectra (fig. S11).

The shape of the 3-μm band observed for the target impacted by the hydrated projectile is indicative of -OH groups, together with a possible contribution from molecular water. The position of the absorption maxima around 2.80 μm is diagnostic of -OH rather than adsorbed molecular water that displays absorption maxima typically longward of 2.95 μm. The overall shape of the 3-μm band in the impact glass in the crater produced by hydrated impact projectiles is very similar to observations of OH-bearing silicate glasses including obsidian (Fig. 6).

DISCUSSION
Metal-rich objects
Metal-rich objects belonging to the Tholen "M-type" or to the Bus-DeMeo "X-complex" taxonomic class (36, 37) show a diversity in spectral behavior (14, 16, 17, 20), characterized by moderate albedos and red-sloped VIS-NIR spectra. Recent high-resolution spectroscopic observations in the VIS-NIR region have shown, however, that the spectra of several M-type asteroids, including (16) Psyche, i.e., the target of the NASA Discovery Psyche mission (22), are not

uniformly featureless as previously believed. The presence of absorption features at about 0.9 μm have been attributed to anhydrous mafic silicates, mainly orthopyroxenes, while absorptions at 0.49 μm and/or in the 2- to 4-μm region have been ascribed to various types of OH- and/or H_2O-bearing phyllosilicate phases (14–17, 38). Mid-infrared observations confirm that Psyche's 7- to 14-μm emissivity spectrum is consistent with the presence of fine-grained (<75 μm) silicates on Psyche's surface (17). From these observations, it has been suggested that Psyche and other M-type asteroids showing the same spectral features are covered by a fine silicate regolith, which may also contain iron grains, overlying an iron-rich bedrock. Heterogeneity in the metal/silicate ratio of the regolith is generally deduced when rotational spectral variations are observable (20, 38). The upper regolith of M-type asteroids is thus inferred to be an exogenous fine-grained material, implanted by low-velocity collisions with silicate-rich asteroids, possibly hydrated such as carbonaceous chondrite Ivuna-type (CI) or Mighei-type (CM) analogs (23, 31, 38).

Because the interpretation of VIS-NIR spectra for M-class objects is subtle, radar is a complementary tool for identifying metallic content in the upper meter or so of the regolith. In the case of Psyche, mean radar albedo of 0.37 ± 0.09 is consistent with a near-surface regolith composed largely of iron-nickel and ~40% porosity (39). Its radar reflectivity varies by a factor of 1.6 as the asteroid rotates, suggesting similarly global variations in metal abundance or bulk density in the near surface—a likely proxy for Fe-Ni metal content.

In the main asteroid belt, metal-rich objects with slower Yarkovsky drift rates than stony objects have much longer collisional lifetimes than stony ones (40). They drift farther from their formation site
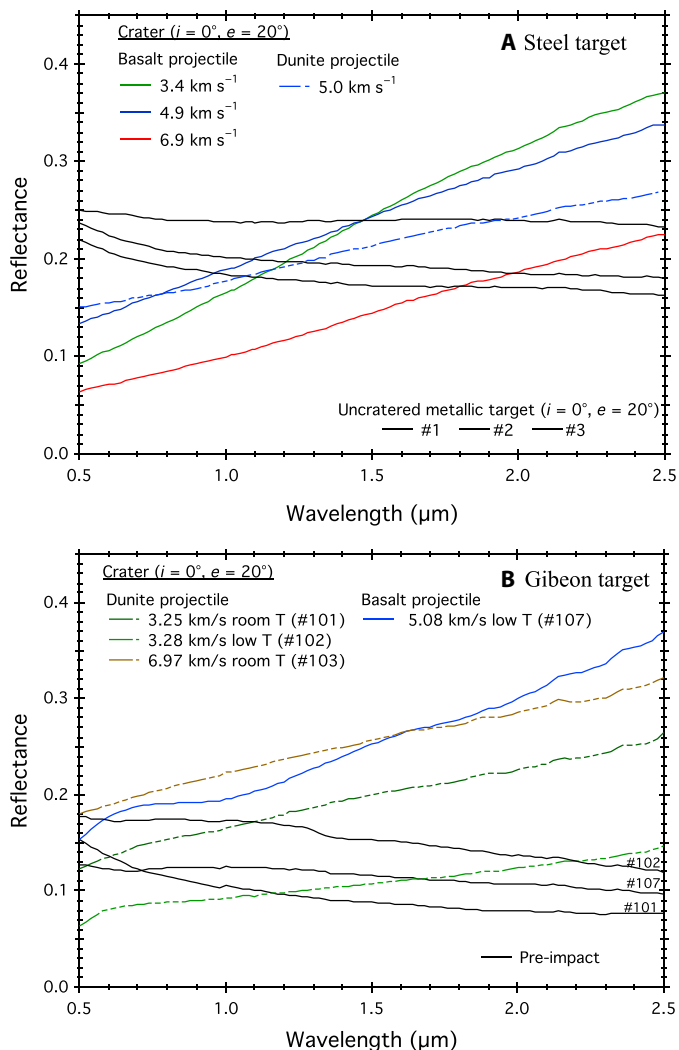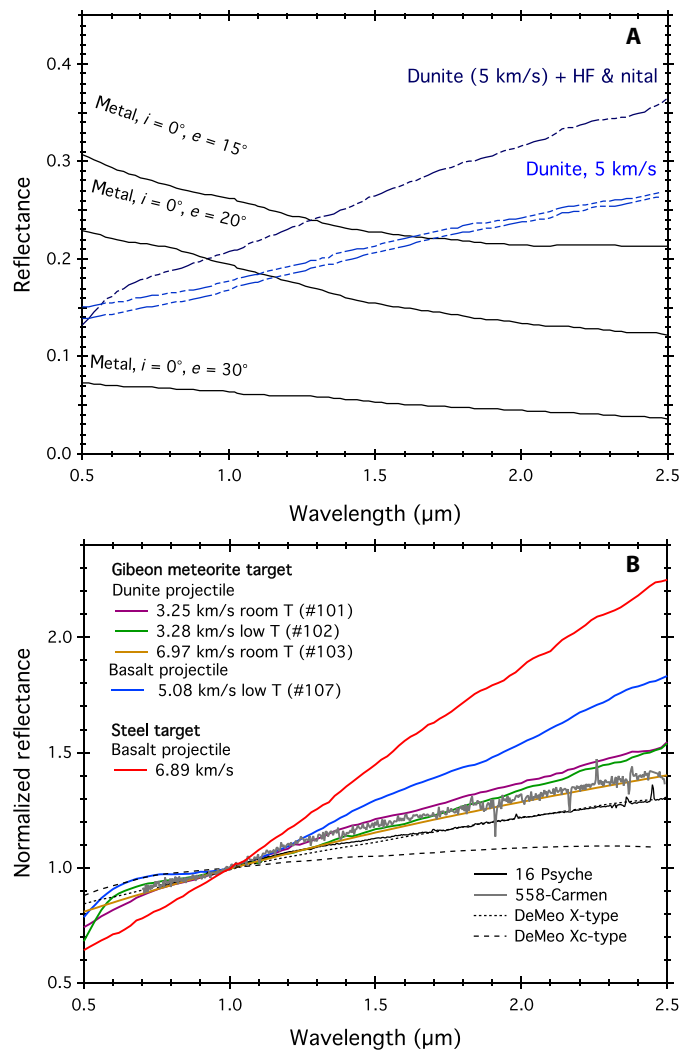
Fig. 4. VIS-NIR spectra of the produced craters. (**A**) Impact experiments performed on a steel target with basaltic (colored solid lines) and dunite projectiles (dashed-dotted line). The spectra of the target outside of the crater are displayed in black. (**B**) Impact experiments performed on the iron meteorite Gibeon with basaltic (blue line) and dunite projectiles (dashed-dotted lines). Note the appearance of broad absorption bands around 1 and 1.9 μm for the craters produced with the basaltic projectile. The spectra of the target outside of the crater are in black. All spectra in (A) and (B) were measured at an incidence of 0° and an emergence of 20°. See table S1 for run conditions.

Fig. 5. VIS-NIR spectra of the produced craters compared to observation of probable metal-rich asteroids. (**A**) VIS-NIR spectra of the craters produced with a dunite projectile, run n5 at 4.91 km/s. The black spectra show the spectral signature of the metal outside of the crater and its dependency on observation geometry (same incidence angle, 0°; three different emergence angles, 15°, 20°, and 30°). The light blue spectra were measured inside the crater (incidence, 0°; emergence, 20°). The dark blue spectra were measured after treating the sample with HF-nital, removing the material coating the crater floor (i.e., glassy dunite). The removal of this material induces an increase of the overall reflectance level. (**B**) Normalized reflectance spectra of the craters produced in this study compared to observation of probable metal-rich asteroid (*14*) as well as metal-related spectral end-members (*36*). The obtained craters show variations of spectral slopes, including slope values similar to ground-based observation of probable metal-rich asteroids.

and typically survive for time scales ranging from a few billion years to several hundred million years, in agreement with their cosmic ray exposure ages (*9*). Meanwhile, the high rate of meteoroid impacts per unit time and unit surface, i.e., on average 10 times higher on the main belt asteroids than on near-Earth asteroids or the Moon (*41*), suggests that surfaces of (large) iron-rich bodies should be crater-saturated. In this context, the cratered surfaces produced in the presented set of hypervelocity impact experiments help in understanding the evolution of iron-rich body surfaces.

Formation of impact melts

The main result of this study is that coating of metallic surfaces by basaltic-like impact melts occurs for typical asteroid belt impact speeds

(≈5 km/s) and does not require less likely low-velocity impact scenarios. We thus propose that glassy coating is a generic outcome of typical impacts experienced by any metal-rich asteroid in the belt. Leading to a camouflage, this would offer a way to bias the interpretation of spectral observations against a high abundance of metal-rich asteroids.

Irrespective of the nature of the projectile, e.g., glassy or crystallized ($T_{\text{glass transition}} \approx 1000$ K basalt; $T_{\text{liquidus}} \approx 1700$ to 2000 K dunite) and, by analogy, for any chondritic or achondritic materials, hydrated or not, impact melting, as shown by our experiments, will alter the
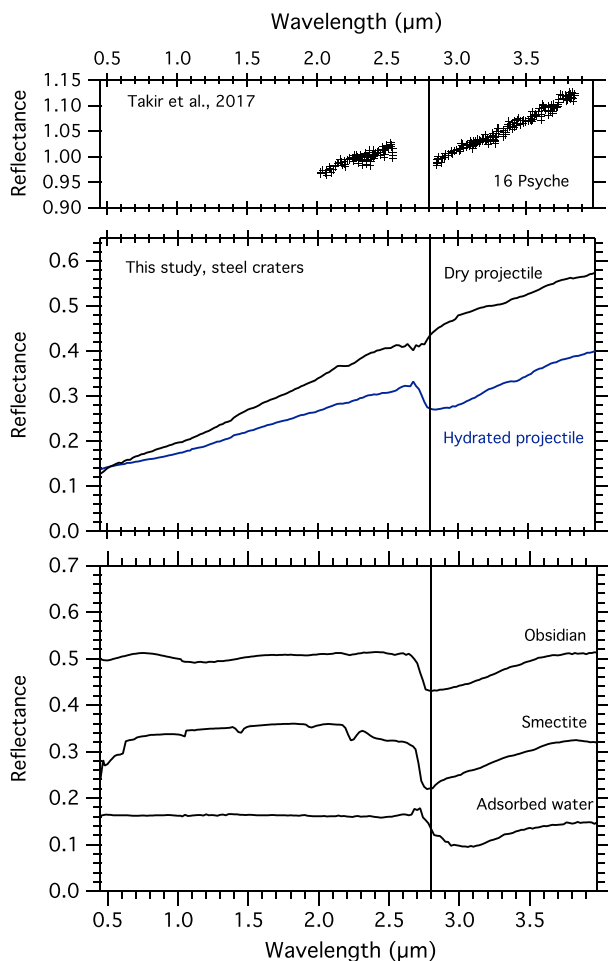
Fig. 6. VIS-NIR reflectance spectra of craters resulting from impact experiments (5.4 km/s) using a dry (ND1) or a wet (NW2) basalt. The clear occurrence of a 3-μm absorption band only in the NW2 crater indicates the entrapment of water, very likely in the form of hydroxyl, within impact glasses. (16) Psyche NIR (*37*) and obsidian, smectite, and condensed water spectra are given for comparison.

metallic signature of the asteroid in response to the very high kinetic energy involved. In the case of small (laboratory scale) impacts, i.e., very short timing (few microseconds) for the post-shock processes, the cooling rate of the impact melt due to adiabatic decompression will be fast enough for the coating to remain glassy—these conditions being closed to those of hyper-quench ($\approx 10^5$ to 10^6 K s^{-1}). The most common way to quantify the glass-forming ability is the critical cooling rate R_c, which is the minimum cooling rate at which a liquid can be frozen to a solid glass without crystallization or with a percentage of crystals below 1 volume % (*42*). Critical cooling rates, being in the order of $R_c \approx 1$ to 10^3 K s^{-1} for basaltic and ultramafic (dunite-like) rocks (*42*), suggest unambiguously that impact melts remain glassy for small hypervelocity impacts, as also suggested by the occurrence of agglutinates on the Moon. The adiabatic decompression paths of impact melts additionally lead to the formation of highly vesicular, foamy, impact glasses in response to the quenching of a melt-gas mixture. These vesicular impact glasses are very similar to their vesicular and slaggy terrestrial analogs, such as Darwin glass (Tasmania) or Aouelloul glass (Mauritania). In the case of larger (beyond laboratory scale) impacts for which post-shock processes

could last much longer, i.e., several seconds, cooling rates could be low enough to promote partial crystallization of the impact melt, possibly with well-developed quench textures of highly elongated (e.g., orthopyroxene) crystals by analogy with terrestrial impact melt (e.g., Vredefort structure, South Africa). In the latter, the nature of the mafic crystallizing phases, i.e., the pyroxene-to-olivine ratio, will depend on the bulk composition (e.g., Mg + Fe/Si ratio) of the projectile, the degree of undercooling, and the cooling rate.

Understanding metal-rich asteroid surfaces

While the spectra of some metal-rich asteroids have been interpreted as being covered by a fine-grained silicate regolith overlying an iron-rich bedrock (*14–20*), the results of our investigation offer an alternative: the presence of glassy coating on impact-related depressions on highly reflective surfaces.

As a result of its darkening ability (Figs. 1 to 3), a basalt-like glassy coating has, first, a drastic effect on decreasing the overall reflectance of reflective iron-rich surfaces and their visible albedo. Depending on the efficiency of impact melt to coat the surface and the thickness of the coating (Figs. 1 and 2), albedo at 0.55 μm of steel or iron meteorite surfaces can be reduced by 15% up to 55% in the presence of basalt/dunite-like glassy coating, taking as a reference the surface of a crater in which the glassy coating has been removed (Fig. 5A). All spectra measured for different impact velocities are red sloped, and impact velocities as well as impactor physicochemical properties (e.g., composition and viscosity) have an influence on the overall reflectance (Fig. 4). In the case of basaltic projectiles on steel, higher impact speeds result in lower albedos and much more reduced spectral slopes, indicating an effective coating by projectile material: Higher impact velocities tend to blur the metallic signatures (Fig. 4). This effect could be enhanced, as in "lunar-like space weathering," by the presence of efficiently absorbing minute metal blebs within the coating material (Fig. 1 and sections S3 and S4) (*43*).

When we look at the VIS-NIR spectral slope, as expressed by the 1.8/0.8-μm reflectance ratio, for instance, slope increases are generally associated with the following parameters: (i) decrease in particle size for powders, (ii) decrease in phase angle for intermediate and smooth slabs, and (iii) increase in roughness for slabs (*44*). In our particular case, the slope increase is very likely due to the increase in roughness of impact-related depressions, as demonstrated by the increase of 1.8/0.8-μm reflectance ratio when the glassy coating is removed from the bottom of the crater (Fig. 5A). Smoothing the roughness of impact-related depressions on impact glassing coating makes them look like smooth slabs (*44*) and thus has a notable effect of making VIS-NIR spectra less red sloped. This finding is further confirmed when basalt and dunite impact crater spectra (Fig. 4B) are considered. Because of their differences in viscosity and wetting properties, dunite impact melts more efficiently coat metallic surfaces than basalt ones (Fig. 2, E and F). The resulting lower roughness of dunite glassy coated surfaces after quenching explains why dunite impact crater spectra are less red sloped than those acquired on basalt craters.

By analogy, these experiments help in understanding the diversity in spectral behavior of iron-rich asteroids (Fig. 4B) (*14–17*). We propose that VIS-NIR spectral variations recorded by iron-rich asteroids could result from a camouflage effect and the ability of impact melts to more or less efficiently coat their surfaces. Following this assertion, coating-free cratered depressions on iron-bedrock should be characterized by rough surfaces and featureless steep red-sloped

spectra over the 0.5- to 2.5-μm range (Fig. 5A). In comparison, similar surfaces coated by basalt-like impact melt should be characterized by red-sloped spectra with lower overall reflectance and lower infrared spectral continuum slope (more blue sloped) in response to their surfaces looking more like smooth slabs. It is clear, however, that the putative formation of a particulate regolith by subsequent impacts on iron-rich asteroids is not taken into account in this discussion (see below).

Fe-bearing glass exhibiting two distinct absorption bands at wavelengths between 1.07 and 1.20 μm, and a second, weaker, centered near 2 μm (34, 35, 45), and very likely attributable to Fe^{2+} in a roughly octahedral coordination environment bound to oxygens associated with silica tetrahedra networks, could theoretically help us to confirm the presence of glassy coating on iron-rich asteroid surfaces. It may be possible to separate olivine from pyroxene from glass by accounting for the fact that they have absorption bands in different wavelength regions (46). As shown by our basalt and dunite glassy coating spectra (Figs. 3 and 4), Fe-bearing glass can be detected but is, however, a weak absorber in the VIS-NIR range and is thus difficult to identify on an asteroid surface, even at high abundances. For this reason, it is also possible that some glass-rich deposits on M-type asteroids, characterized by almost featureless red-sloped spectra, have been misidentified, causing glass occurrences on small body surfaces to be underreported. More work needs to be done in these new directions.

Indirect occurrence of glassy materials at the surface of iron-rich asteroids could also be inferred from absorption bands of mafic silicates in several spectra of M-type asteroids. Up to now, emissivity spectra have been interpreted by the presence of (exogenous) fine-grained silicate regolith on iron-rich asteroid surfaces (17). However, the occurrence of partly crystallized glassy materials resulting from partial crystallization due to more or less rapid cooling of impact melts could not be ruled out. Minitti et al. (45) have shown that, in the VIS-NIR and mid-IR wavelength ranges, increasing crystallization is accompanied by an increasing influence of pyroxene absorptions and decreasing influence of glass absorptions—the orthopyroxene being a strong absorber. The only major effect of glass at abundances below 80% is to widen and skew the 1-μm absorption band toward longer wavelengths, a feature that can be tentatively seen in several M-type asteroids showing only a faint or no 1.9- to 2-μm absorption (16, 20). This effect is, however, subtle even at high abundances, and glass + mafic mineral mixture spectra look qualitatively very similar to spectra of only mafic minerals [e.g., olivine + orthopyroxene mixtures for mid-IR spectra of (16) Psyche; (17)]. Therefore, we suggest that more or less recrystallized glassy coatings could be present in significant quantities on several M-type asteroid surfaces and still not be readily detected using VIS-NIR spectroscopy.

The cooling rate of the material heated by the impact should depend on the size of the impactor, i.e., the scale of the impact event. For larger impact events, the probability of crystal formation (e.g., orthopyroxene and olivine) instead of pure glassy materials increases. However, the larger the impactor size, the less frequent the impact; therefore, the surface features produced by the larger and statistically rarer events are modified and repainted by the more frequent smaller impact events. The presence in all of the spectra of several iron-rich asteroids including (16) Psyche of a weak orthopyroxene absorption band (circa 0.9 μm) could be consistent with this assertion, which, in this case, would suggest a non-endogenous origin for this silicate component.

On the Moon, impact melting has been seen in craters several hundred meters in diameter (47). On asteroid Vesta, small flow-like surface features have been found, suggesting a possible impact origin (48). Generally, it is difficult to melt materials in main belt collisions in the asteroid main belt, because the average collision speed is lower than that onto the Moon. However, as shown in this study, collisions on metal objects generate higher shock pressures than silicate-silicate collisions so that the melting of the impactor becomes easier. Surface spectroscopic mapping of the Psyche mission will reveal how past impact processes of metallic bodies, i.e., past impact events, have changed the surface and spectra of metallic bodies.

Last, by showing the preservation of a hydrated glass coating on the surface of a metal-rich target after impact conditions (Fig. 6 and fig. S11), the present results demonstrate that one of the most volatile compounds can be preserved despite the high kinetic energy involved in impact processes typical of the main asteroid belt. These findings challenge the classical view according to which the detection of a 3-μm absorption band on M-type asteroids must be restricted to exogenous OH- and/or H_2O-bearing minerals implanted by low-impact collisions. They also open up the interesting perspective that iron-rich asteroids could be vectors of water transport in the main asteroid belt and that, like as planetary materials do (24, 25, 49), impact cratering on iron-rich asteroids, including (16) Psyche, would keep track not only of hydrated projectiles, which could correspond to carbonaceous chondrites, but also of some water-rich asteroids. In this perspective, it remains, however, to be verified whether the hydration is related to the size of the M-type asteroids (15), i.e., the ones larger than 65 km being likely to be hydrated and the smaller ones being anhydrous.

Is camouflage of iron-rich asteroids consistent with other remote measurements?

Although much higher than that of other asteroids of comparable size, the thermal inertia of M-type asteroids is much lower than that of solid metal iron. Taking (16) Psyche as a representative example, its recent estimates of thermal inertia of 114 to 133 ± 40 J m^{-2} K^{-1} $s^{-1/2}$ (50) and 80 to 95 J m^{-2} K^{-1} $s^{-1/2}$ or 5 to 25 J m^{-2} K^{-1} $s^{-1/2}$ (17) are much very low, as values for iron and iron-rich materials can be as high as 16,700 and 12,000 J m^{-2} K^{-1} $s^{-1/2}$. While both studies used different datasets and techniques (i.e., interferometry versus spectroscopy), they both show that Psyche has a low macroscopic surface roughness, which is consistent with a boulder-free, metal-rich bedrock, covered by a very small average particle size silicate regolith (<75 μm) (17).

In addition to the occurrence of a particulate regolith, this relatively low thermal inertia of M-type asteroids may also be due to the vesicularity and the formation of foamy carapace (Fig. 3) in response to adiabatic decompression paths of impact melts. Laboratory measurements of thermal conductivity and physical properties for Hawaiian basalts (51, 52) have shown that thermal inertia is inversely proportional to porosity and/or vesicularity. For instance, a basalt-like frozen impact melt with a representative value of 2500 J m^{-2} K^{-1} $s^{-1/2}$ (53) drops its thermal inertia by almost an order of magnitude down to values lower than 250 to 200 J m^{-2} K^{-1} $s^{-1/2}$ by increasing its vesicularity to that of a typical pumice (>75 to 80% vesicles). This effect could be even more pronounced on asteroids by impacting the bulk thermal conductivity if vesicle gas pressures are assumed to be well lower. Because these values of thermal inertia are almost similar to the range measured for large M-type asteroids—(16) Psyche

(17, 50), (22) Kalliope, or (216) Kleopatra (54)—highly vesicular glassy coatings on smooth iron-rich asteroid surfaces should thus be considered as a plausible alternative for producing low thermal inertia surfaces on an otherwise highly conductive metal-rich bedrock.

Using the S-band radar at the Arecibo Observatory, it was found that (16) Psyche and some other M-type asteroids have large- and small-scale variations in their surface bulk density. Interpreted as isolated patches of metal- and silicate-rich regions at the near surface, these radar reflectivity variations may result from collisions between metal- and silicate-rich asteroids (23, 39). Similarly, Ockert-Bell et al. (20) found evidence of a correlation between radar reflectivity and infrared spectral continuum slope, indicating that objects with higher radar albedos tend to have steeper sloped continua. These variations in radar albedo are consistent with the present findings and show that cratering is very likely an important process controlling the surface evolution of metal-rich asteroids. In addition to low-density glassy coatings, the decrease in target's density produced by spallation and fracturation during the excavation stage of crater formation together with the propagation of impact melts at depth (Fig. 1) may offer a complementary explanation for the low bulk density of near-surface iron-rich asteroids compared to the metal/alloy density.

Last, many of the M-type asteroids show spectral rotational variations accompanied by changes in overall reflectance and slope variations in the near infrared (20). As demonstrated by a reflectance survey on iron meteorite slabs and powders (33, 44), these spectral changes do not necessarily require drastic changes in surface properties to account for these variations. Spectral variations are accommodated more readily by small changes in the roughness and viewing geometry of iron meteorite slabs than small changes in viewing geometry or grain size of iron meteorite powders. While this may hold for small-scale samples in the laboratory, asteroid spectra are integrated over the entire visible face, and these changes are very likely averaged over all the contributing viewing geometries. It seems, therefore, that if some impact-generated smooth glassy silicate coating may be retained, then other areas of the same M-type asteroid could host a particulate regolith composed of these impact products that have degraded and later been dislodged and shattered by subsequent impacts during their long collisional lifetime in the belt; metal spalls and other unprocessed target and projectile materials could well be produced by impacts on an iron surface depending on the impact angle [section S1; (30, 55)].

Is there a deficit of iron-rich asteroids?

A deficit of metal-rich objects in the main belt is often inferred from the detection of only a few asteroids in the M taxonomic class by spectral analysis and radar reflectivity. From this set of impact experiments, we suggest that this deficit is only apparent. It results from the coating of metallic surfaces by silicate melts produced during impacts of projectiles of various compositions with speeds typical of those occurring in the asteroid belt. Spectral analysis of our metallic targets after impact shows that the optical signature of metal is profoundly modified. This analysis may also apply to hypervelocity impacts into other kinds of asteroids with high content of microscale porosity, as more shock energy is absorbed close to the impact site and converted into heat on a porous asteroid by permanent crushing of pore space (56). Depending on how much heating is produced during this process, coating could also occur and hide the original surface composition at the impact site (25, 49).

There are several reasons why iron-rich asteroid surfaces must differ from the texture of the regolith of silica-rich stony asteroids. These include (i) the much longer collisional lifetimes of iron-rich asteroids than stony ones, (ii) the ease of melting simultaneously part of the Fe-Ni alloy targets by silicate projectiles during high–kinetic energy impact events, (iii) the occurrence of silicate-iron immiscible liquid in impact melts (Fig. 3), and (iv) the quenching of the silicate melt mixtures into vesicular (possibly hydrated) glassy coatings during the adiabatic decompression path of impact melts. The surface of a large iron-rich asteroid such as (16) Psyche must be composed of smooth impact-related depressions, consistent with a metal-rich bedrock, and covered from place to place by a highly vesicular, partially crystallized, hydrated or not glassy coating and by a heterogeneous particulate regolith composed of both metallic and silicate materials. If not combined with radar observations that can strongly indicate whether a body is metal-rich, spectral observations from the ground can be deceiving to identify metal-rich bodies in the asteroid belt. The Psyche mission in the NASA Discovery program to be launched in 2022 to visit the asteroid (16) Psyche offers a unique opportunity to obtain direct information on the surface properties of a large metal-rich asteroid and to test the predictions of this study, in particular, the relative abundance of regolith and glassy coated surfaces and their important implications in our understanding of metal-rich asteroids.

MATERIALS AND METHODS
Hypervelocity experiments
Impact experiments were performed using a 7-mm bore two-stage light-gas gun at the Institute of Space and Astronautical Science (ISAS) in Japan. Spheroidal or cylindrical projectiles of about 3 mm in diameter were all shot vertically to the target surface using a plastic sabot (24). Experiments were performed in a range of impact speeds between 3 and 7 km/s, allowing the determination of the scaling of the outcome with impact speed (see table S1). A square aluminum witness plate of side 28 cm with a central hole 4 cm in diameter allowing the projectile to go through was placed in front of the target. Aluminum small plates of the order of centimeters in width were fixed on the aluminum witness plate. These plates were used to collect ejecta from the impact. The distance between the witness plate and the target surface was about 10 cm (fig. S1). All the experiments were performed under vacuum condition (<10 Pa) and at room temperature, unless specified in table S1. Eleven experimental runs were performed with increasing impact speed (from 3.39 to 6.89 km/s) and different masses of dry and wet, glassy, or fully crystallized projectiles (from 0.03 to 0.1 g), resulting in different impact energies (from 190 to 1899 J; see table S1). Projectile and ejecta trajectories are captured with a high-speed video camera (frame rate of 2 or 4 μs) that monitors the experiment.

Samples
Projectiles
Chondrites and achondrites from our meteorite collections were not enough cohesive materials to be accelerated to 5 km/s and too much heterogeneous at an infra-millimeter scale, so we considered both glassy [i.e., a phonolitic aphanitic lava (n0 to n5 series), Yakuno basalt (n107), and a dry (ND1) and wet (NW2) PST9 basalt from Pichavant et al. (57)] and fully crystallized materials [i.e., Higasiakaisiyama dunite (n101 to n103 series)] to mimic the diversity of asteroid projectile

materials (table S1). The rock projectiles (basalt and dunite) were cut from the leftover samples of previous experiments from previous impact experiments (*58, 59*).

Targets

Both steel and iron meteorite materials have been used as targets for these hypervelocity experiment runs to take into account the differences in the thermodynamic and mechanical properties of the two metals. The steel targets consisted of SCM 435 steel cylinders (5 to 6 cm radius and 3 to 4 cm height) and have a composition circa Fe (96.86 to 97.87 wt %), Cr (0.9 to 1.2 wt %), Mn (0.6 to 0.85 wt %), C (0.33 to 0.38 wt %), Si (0.15 to 0.35 wt %), and Mo (0.15 to 0.3 wt %). Gibeon, an iron meteorite belonging to IVA Iron (7.93% Ni, 0.41% Co, 0.04% P), was selected to serve as a proxy of metal-rich asteroids. Gibeon is a polycrystalline, twinned, fine octahedrite, with a bandwidth of 0.30 ± 0.05 mm. Etched sections display a fine Widmanstätten structure of straight, long kamacite lamellae with a width of 0.30 ± 0.05 mm. The kamacite shows Neumann bands and subboundaries and has a hardness of 170 ± 10. Gibeon belongs to those meteorites that display a very pure metallic matrix. Chunks of about 3 to 5 cm of Gibeon polished on one side were used as targets.

Analytical

The description of target, craters, and their coating were performed using both a benchtop scanning electron microscope (COXEM EM-30PLUS, UCA, Lagrange) and a scanning electron microscope (Philips FEI XL30 ESEM LaB6) equipped with a Quantax 655 detector (Bruker), operated at 20-kV and 200-nA beam current at Centre de Mise en Forme des Matériaux–Mines ParisTech. Both secondary and back-scattered electron modes have been used for images. Energy-dispersive x-ray diffraction analyses were used to analyze the coating and target compositions. Chemical maps were acquired for each crater to discern the difference between the impact melt and the crater floor of the metallic target. VIS-NIR spectra of the crater floor of the metallic target were acquired for each impact experiments with a spectro-photo-goniometer available at Institut de Planétologie et d'Astrophysique de Grenoble. This instrument uses a Globar light source coupled to a monochromator to illuminate the target material. The reflected light was measured using a silicon (visible to 1 μm) and a cryo-cooled InSb detector (1 to 4.8 μm). We used a modified version of the setup. A spherical mirror was inserted in the optical path to produce a focused illumination of 7 mm diameter. Spectra were normalized to spectralon (up to 2.4 μm) and infragold (2.4 to 2.6 μm). The typical photometric accuracy of the setup is of 0.5%, as tested using replicate measurements on a dark reference (5% reflectance). Measurements were done using a nadir illumination (incidence, 0°) and phase angles below 30° to mimic asteroid observations. Reflectance spectra were not measured under ambient pressure in a cold room ($T = -10°C$). The use of a cold room minimizes contribution from adsorbed water. Except in the case of experiments performed with a hydrated projectile, signatures of hydration at 3 μm were absent from the spectra measured on the metallic targets impacted at room temperature.

SUPPLEMENTARY MATERIALS

REFERENCES AND NOTES

1. T. Kleine, K. Mezger, H. Palme, E. Scherer, C. Münker, Early core formation in asteroids and late accretion of chondrite parent bodies: Evidence from ^{182}Hf–^{182}W in CAIs, metal-rich chondrites, and iron meteorites. *Geochim. Cosmochim. Acta* **69**, 5805–5818 (2005).
2. T. S. Kruijer, M. Touboul, M. Fischer-Gödde, K. R. Bermingham, R. J. Walker, T. Kleine, Protracted core formation and rapid accretion of protoplanets. *Science* **344**, 1150–1154 (2014).
3. G. Libourel, P. Michel, M. Delbo, C. Ganino, A. Recio-Blanco, P. de Laverny, M. E. Zolensky, A. N. Krot, Search for primitive matter in the Solar System. *Icarus* **282**, 375–379 (2017).
4. C. T. Russell, C. A. Raymond, A. Coradini, H. Y. McSween, M. T. Zuber, A. Nathues, M. C. De Sanctis, R. Jaumann, A. S. Konopliv, F. Preusker, S. W. Asmar, R. S. Park, R. Gaskell, H. U. Keller, S. Mottola, T. Roatsch, J. E. C. Scully, D. E. Smith, P. Tricarico, M. J. Toplis, U. R. Christensen, W. C. Feldman, D. J. Lawrence, T. J. McCoy, T. H. Prettyman, R. C. Reedy, M. E. Sykes, T. N. Titus, Dawn at Vesta: Testing the protoplanetary paradigm. *Science* **336**, 684–686 (2012).
5. W. Neumann, D. Breuer, T. Spohn, Differentiation of Vesta: Implications for a shallow magma ocean. *Earth Planet. Sci. Lett.* **395**, 267–280 (2014).
6. T. H. Burbine, T. J. McCoy, A. Meibom, B. Gladman, K. Keil, Meteoritic parent bodies: Their number and identification, in *Asteroids III*, W. F. Bottke Jr., A. Cellino, P. Paolicchi, R. P. Binzel, Eds. (University of Arizona Press, 2002), pp. 653–667.
7. J. I. Goldstein, E. R. D. Scott, N. L. Chabot, Iron meteorites: Crystallization, thermal history, parent bodies, and origin. *Geochemistry* **69**, 293–325 (2009).
8. E. R. D. Scott, J. T. Wasson, Classification and properties of iron meteorites. *Rev. Geophys.* **13**, 527–546 (1975).
9. O. Eugster, G. F. Herzog, K. Marti, M. W. Caffee, Irradiation records, cosmic-ray exposure ages, and transfer times of meteorites, in *Meteorites and the Early Solar System II*, D. S. Lauretta, H. Y. McSween Jr., Eds. (University of Arizona Press, 2006), pp. 829–851.
10. C. R. Chapman, J. W. Salisbury, Comparisons of meteorite and asteroid spectral reflectivities. *Icarus* **19**, 507–522 (1973).
11. M. J. Gaffey, Spectral reflectance characteristics of the meteorite classes. *J. Geophys. Res.* **81**, 905–920 (1976).
12. J. F. Bell, D. R. Davis, W. K. Hartmann, M. J. Gaffey, Asteroids: The big picture, in *Asteroids II*, R. P. Binzel, T. Gehrels, M. S. Matthews, Eds. (University of Arizona Press, 1989), pp. 921–948.
13. E. A. Cloutis, M. J. Gaffey, D. G. W. Smith, R. S. J. Lambert, Metal silicate mixtures: Spectral properties and applications to asteroid taxonomy. *J. Geophys. Res.* **95**, 8323–8338 (1990).
14. P. S. Hardersen, M. J. Gaffey, P. A. Abell, Near-IR spectral evidence for the presence of iron-poor orthopyroxenes on the surfaces of six M-type asteroids. *Icarus* **175**, 141–158 (2005).
15. A. S. Rivkin, E. S. Howell, L. A. Lebofsky, B. E. Clark, D. T. Britt, The nature of M-class asteroids from 3-micron observations. *Icarus* **145**, 351–368 (2000).
16. S. Fornasier, B. E. Clark, E. Dotto, Spectroscopic survey of X-type asteroids. *Icarus* **214**, 131–146 (2011).
17. Z. A. Landsman, J. P. Emery, H. Campins, J. Hanuš, L. F. Lim, D. P. Cruikshank, Asteroid (16) Psyche: Evidence for a silicate regolith from spitzer space telescope spectroscopy. *Icarus* **304**, 58–73 (2018).

18. M. K. Shepard, B. E. Clark, M. C. Nolan, E. S. Howell, C. Magri, J. D. Giorgini, L. A. M. Benner, S. J. Ostro, A. W. Harris, B. Warner, D. Pray, P. Pravec, M. Fauerbach, T. Bennett, A. Klotz, R. Behrend, H. Correia, J. Coloma, S. Casulli, A. Rivkin, A radar survey of M- and X-class asteroids. *Icarus* **195**, 184–205 (2008).

19. M. K. Shepard, B. E. Clark, M. Ockert-Bell, M. C. Nolan, E. S. Howell, C. Magri, J. D. Giorgini, L. A. M. Benner, S. J. Ostro, A. W. Harris, B. D. Warner, R. D. Stephens, M. Mueller, A radar survey of M- and X-class asteroids II. Summary and synthesis. *Icarus* **208**, 221–237 (2010).

20. M. E. Ockert-Bell, B. E. Clark, M. K. Shepard, R. A. Isaacs, E. A. Cloutis, S. Fornasier, S. J. Bus, The composition of M-type asteroids: Synthesis of spectroscopic and radar observations. *Icarus* **210**, 674–692 (2010).

21. W. F. Bottke, D. Nesvorný, R. E. Grimm, A. Morbidelli, D. P. O'Brien, Iron meteorites as remnants of planetesimals formed in the terrestrial planet region. *Nature* **439**, 821–824 (2006).

22. L. T. Elkins-Tanton, E. Asphaug, J. Bell, D. Bercovici, B. G. Bills, R. P. Binzel, W. F. Bottke, I. Jun, S. Marchi, D. Oh, C. A. Polanskey, B. P. Weiss, D. Wenkert, M. T. Zuber, Journey to a metal world: Concept for a discovery mission to Psyche, in *45th Lunar and Planetary Science Conference* (Lunar and Planetary Institute, 2014), pp. 1253.

23. M. K. Shepard, P. A. Taylor, M. C. Nolan, E. S. Howell, A. Springmann, J. D. Giorgini, B. D. Warner, A. W. Harris, R. Stephens, W. J. Merline, A. Rivkin, L. A. M. Benner, D. Coley, B. E. Clark, M. Ockert-Bell, C. Magri, A radar survey of M- and X-class asteroids. III. Insights into their composition, hydration state, and structure. *Icarus* **245**, 38–55 (2015).

24. V. Reddy, L. L. Corre, D. P. O'Brien, A. Nathues, E. A. Cloutis, D. D. Durda, W. F. Bottke, M. U. Bhatt, D. Nesvorny, D. Buczkowski, J. E. C. Scully, E. M. Palmer, H. Sierks, P. J. Mann, K. J. Becker, A. W. Beck, D. Mittlefehldt, J.-Y. Li, R. Gaskell, C. T. Russell, M. J. Gaffey, H. Y. McSween, T. B. McCord, J.-P. Combe, D. Blewett, Delivery of dark material to Vesta via carbonaceous chondritic impacts. *Icarus* **221**, 544–559 (2012).

25. R. T. Daly, P. H. Schultz, Predictions for impactor contamination on Ceres based on hypervelocity impact experiments. *Geophys. Res. Lett.* **42**, 7890–7898 (2015).

26. W. F. Bottke Jr., M. C. Nolan, R. A. Kolvoord, R. Greenberg, Velocity distribution among colliding asteroids. *Icarus* **107**, 255–268 (1994).

27. C. Ganino, G. Libourel, A. M. Nakamura, S. Jacomet, O. Tottereau, P. Michel, Impact-induced chemical fractionantion as inferred from hypervelocity impact experiments with silicate projectiles and metallic targets. *Meteorit. Planet. Sci.* **53**, 2306–2326 (2018).

28. N. Kawai, K. Tsurui, S. Hasegawa, E. Sato, Single microparticle launching method using two-stage light-gas gun for simulating hypervelocity impacts of micrometeoroids and space debris. *Rev. Sci. Instrum.* **81**, 115105 (2010).

29. M. J. Burchell, N. G. Mackay, Crater ellipticity in hypervelocity impacts on metals. *J. Geophys. Res.* **103**, 22761–22774 (1998).

30. F. Hörz, Cratering and penetration experiments in aluminum and Teflon: Implications for space-exposed surfaces. *Meteorit. Planet. Sci.* **47**, 763–797 (2012).

31. R. T. Daly, P. H. Schultz, Projectile preservation during oblique hypervelocity impacts. *Meteorit. Planet. Sci.* **53**, 1364–1390 (2018).

32. T. Moritoh, S. Matsuoka, T. Ogura, G. N. Kazutaka, K.-i. Kondo, M. Katayama, M. Yoshida, Dynamic failure of steel under hypervelocity impact of polycarbonate up to 9 km/s. *J. Appl. Phys.* **93**, 5983–5988 (2003).

33. D. T. Britt, C. M. Pieters, Bidirectional reflectance properties of iron-nickel meteorites, in *Proceedings of the 18th Lunar and Planetary Science Conference* (Cambridge Univ. Press/ Lunar and Planetary Institute, 1988), pp. 503–512.

34. P. M. Bell, H. K. Mao, R. M. Hazen, A. L. Mao, Optical spectra and electron paramagnetic resonance of lunar and synthetic glasses: A study of the effects of controlled atmosphere, composition, and temperature, in *Proceedings of the Seventh Lunar Science Conference* (Pergamon Press, 1976), 2543–2559.

35. E. A. Cloutis, Fe-bearing glassy materials: Spectral reflectance properties, in *46th Planetary Science Conference* (Lunar and Planetary Institute, 2015), pp. 1234.

36. D. J. Tholen, "Asteroid taxonomy from cluster analysis of photometry," thesis, University of Arizona, Tucson, AZ (1984).

37. F. E. DeMeo, R. P. Binzel, S. M. Slivan, S. J. Bus, An extension of the Bus asteroid taxonomy into the near-infrared. *Icarus* **202**, 160–180 (2009).

38. D. Takir, V. Reddy, J. A. Sanchez, M. K. Shepard, J. P. Emery, Detection of water and/or hydroxyl on asteroid (16) Psyche. *Astrophys. J.* **153**, 31 (2017).

39. M. K. Shepard, M. K. Shepard, J. Richardson, P. A. Taylor, L. A. Rodriguez-Ford, A. Conrad, I. Pater, M. Adamkovics, K. Kleer, J. R. Males, K. M. Morzinski, L. M. Close, M. Kaasalainen, M. Viikinkoski, B. Timerson, V. Reddy, C. Magri, M. C. Nolan, E. S. Howell, L. A. M. Benner, J. D. Giorgini, B. D. Warner, A. W. Harris, Radar observations and shape model of asteroid 16 Psyche. *Icarus* **281**, 388–403 (2017).

40. P. Farinella, D. Vokrouhlicky, W. K. Hartmann, Meteorite delivery via Yarkovsky orbital drift. *Icarus* **132**, 378–387 (1998).

41. M. Delbo, G. Libourel, J. Wilkerson, N. Murdoch, P. Michel, K. T. Ramesh, C. Ganino, C. Verati, S. Marchi, Thermal fatigue as the origin of regolith on small asteroids. *Nature* **508**, 233–236 (2014).

42. G. Iezzi, S. Mollo, G. Ventura, Solidification behaviour of natural silicate melts and volcanological implications, in *New Research on Volcanoes: Formation, Eruptions and Modeling*, N. Lewis and A. Moretti, Eds. (Nova Science Publishers, Inc., 2009), pp. 127–151.

43. L. V. Moroz, L. V. Starukhina, S. S. Rout, S. Sasaki, J. Helbert, D. Baither, A. Bischoff, H. Hiesinger, Space weathering of silicate regoliths with various FeO contents: New insights from laser irradiation experiments and theoretical spectral simulations. *Icarus* **235**, 187–206 (2014).

44. E. A. Cloutis, P. S. Hardersen, D. L. Bish, D. T. Bailey, M. J. Gaffey, M. A. Craig, Reflectance spectra of iron meteorites: Implications for spectral identification. *Meteorit. Planet. Sci.* **45**, 304–332 (2010).

45. M. E. Minitti, J. F. Mustard, M. J. Rutherford, Effects of glass content and oxidation on the spectra of SNC-like basalts: Applications to Mars remote sensing. *J. Geophys. Res.* **107**, 5030 (2002).

46. B. H. N. Horgan, E. A. Cloutis, P. Mann, J. F. Bell III, Near-infrared spectra of ferrous mineral mixtures and methods or their identification in planetary surface spectra. *Icarus* **234**, 132–154 (2014).

47. J. D. Stopar, B. R. Hawke, M. S. Robinson, B. W. Denevi, T. A. Giguere, S. D. Koeber, Occurrence and mechanisms of impact melt emplacement at small lunar craters. *Icarus* **243**, 337–357 (2014).

48. D. A. Williams, D. P. O'brien, P. M. Schenk, B. W. Denevi, U. Carsenty, S. Marchi, J. D. Scully, R. Jaumann, M. C. De Sanctis, E. Palomba, E. Ammannito, A. Longobardo, G. Magni, A. Frigeri, C. T. Russell, C. A. Raymond, T. M. Davison, Lobate and low-like features on asteroid Vesta. *Planet. Space Sci.* **103**, 24–35 (2014).

49. R. T. Daly, P. H. Schultz, The delivery of water by impacts from planetary accretion to present. *Sci. Adv.* **4**, eaar2632 (2018).

50. A. Matter, M. Delbo, B. Carry, S. Ligori, Evidence of a metal-rich surface for the asteroid (16) Psyche from interferometric observations in the thermal infrared. *Icarus* **226**, 419–427 (2013).

51. E. C. Robertson, D. L. Peck, Thermal conductivity of vesicular basalt from Hawaii. *J. Geophys. Res.* **79**, 4875–4888 (1974).

52. J. R. Zibelman, The role of porosity in thermal inertia variations on basaltic lavas. *Icarus* **68**, 366–369 (1986).

53. B. M. Jakosky, On the thermal properties of martian fines. *Icarus* **66**, 117–124 (1986).

54. F. Marchis, J. E. Enriquez, J. P. Emery, M. Mueller, M. Baek, J. Pollock, M. Assafin, R. V. Martins, J. Berthier, F. Vachier, D. P. Cruikshank, L. F. Lim, D. E. Reichart, K. M. Ivarsen, J. B. Haislip, A. P. La Cluyze, Multiple asteroid systems: Dimensions and thermal properties from Spitzer Space Telescope and ground-based observations. *Icarus* **221**, 1130–1161 (2012).

55. T. Matsui, P. H. Schultz, On the brittle-ductile behavior of iron meteorites: New experimental constraints. *J. Geophys. Res.* **89**, C323–C328 (1984).

56. E. Asphaug, G. Collins, M. Jutzi, Global-scale impacts, in *Asteroids IV*, P. Michel, F. E. DeMeo, W. F. Bottke, Eds. (University of Arizona Press, 2015), pp. 661–677.

57. M. Pichavant, I. Di Carlo, Y. Le Gac, S. G. Rotolo, B. Scaillet, Experimental constraints on the deep magma feeding system at Stromboli volcano, Italy. *J. Petrol.* **50**, 601–624 (2009).

58. T. Katsura, A. M. Nakamura, A. Takabe, T. Okamoto, K. Sangen, S. Hasegawa, X. Liu, T. Mashimo, Laboratory experiments on the impact disruption of iron meteorites at temperature of near-Earth space. *Icarus* **241**, 1–12 (2014).

59. A. Nakamura, A. Fujiwara, Velocity distribution of fragments formed in simulated collisional disruption. *Icarus* **92**, 132–146 (1991).